Original Research

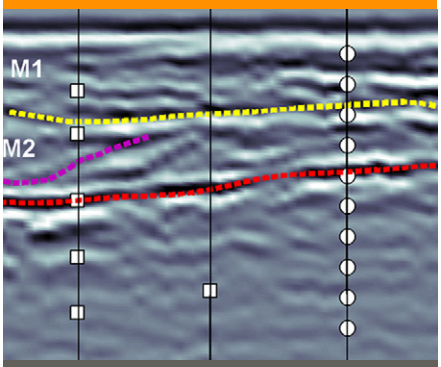

A field-scale infiltration experiment was conducted in coarse conglomeratic soil with high gravel fraction. Unsaturated flow properties were estimated from modeling of infiltration using the van Genuchten–Mualem model and a Metropolis–Hasting optimization scheme. Results provide optimal unsaturated flow parameters for a soil type that is underrepresented for vadose zone flow.

M.J. Thoma, W. Barrash, and J. Bradford, Center for Geophysical Investigation into the Shallow Subsurface and Dep. of Geosciences, Boise State Univ., Boise, ID 83725; M. Cardiff, Dep. of Geoscience, Univ. of Wisconsin, Madison, WI 53706; and J. Mead, Dep. of Mathematics, Boise State Univ., Boise, ID 83725. *Corresponding author (michaelthoma@u.boisestate.edu).

Vadose Zone J.
doi:10.2136/vzj2013.05.0096
Received 29 May 2013.

Estimating Unsaturated Hydraulic Functions for Coarse Sediment from a Field-Scale Infiltration Experiment

Michael J. Thoma,* Warren Barrash, Michael Cardiff, John Bradford, and Jodi Mead

Conglomeratic alluvial sediments (sand–gravel–cobbles) are common in fluvial, periglacial, and tectonically active regions but have received little attention with respect to unsaturated flow, specifically moisture–tension–conductivity relationships, due to difficulty in making measurements in the field or laboratory and lack of agricultural value. We used a field-scale infiltration experiment, a one-dimensional layered forward model, and parameter estimation modeling to examine in situ flow behavior between residual and partial saturation in a four-layer system under steady infiltration (0.84 cm h^{-1}) for 19 h. Prior information from ground-penetrating radar, grain-size distributions from core samples, and long-term tension (ψ) and moisture (θ) monitoring were used to define geologic structure, simulate test behavior, and provide initial parameter estimates. Vertically distributed measurements of $\psi(t)$ and $\theta(t)$ from the experiment were matched using four parameters (θ_s, α, n, and K_s) of the van Genuchten–Mualem (VGM) relationships for each material layer and a Metropolis–Hastings (MH) search with multiple, independent-chain runs to 10^6 samples each. Scale reduction factors indicated convergence of independent chains for 11 of 16 parameters. Final distributions of individual parameters varied from normal to nearly uniform distributions, and some parameter pairs showed high cross-correlation ($R^2 > 0.9$). Results showed that (i) VGM relationships can be applied to these coarse, conglomeratic soils to characterize unsaturated flow behavior across the natural range of partial saturation, (ii) even under high sustained infiltration rates, these coarse conglomeratic soils remain well drained, despite relatively low porosity and significant cobble fraction, and (iii) high uncertainty and nonconvergence of MH chains does not lead to significant misfit of the observed data. These findings imply that a significant cobble fraction does not markedly reduce infiltration at low saturation levels that develop under natural recharge conditions.

Abbreviations: AT, advanced tensiometer; BHRS, Boise Hydrogeophysical Research Site; bls, below land surface; GPR, ground-penetrating radar; MH, Metropolis–Hastings; VGM, van Genuchten–Mualem.

In many arid and semiarid regions, high-energy riparian areas, and large outwash plains, considerable portions of the surface and subsurface are covered by stony soils or coarse (conglomeratic) alluvial sediments that contain significant fractions of large clasts or rock fragments with grain size diameter (d) >2 mm (Miller and Guthrie, 1984; Cousin et al., 2003). These conglomeratic alluvial soils, by which we mean alluvial sediments with composition from sand to gravel to large cobbles (d > 10 cm) with little pedogenesis, have previously received little attention concerning unsaturated flow because they are not well suited for agriculture and are often present in underdeveloped landscapes (e.g., desert, periglacial, and floodplain environments). With recent population increases has come sprawl into regions where these alluvial soils dominate, and there has been an increasing interest in the unsaturated flow properties of these materials.

The presence of rock fragments in soil has been linked to significant alterations to water flow mechanics and soil heat flux in the vadose zone (Cousin et al., 2003), with particular focus given in the fields of contamination and mine waste (Corwin et al., 1999; Dann et al., 2009; Milczarek et al., 2006), radioactive waste storage (Oostrom et al., 2009, 2011; Tokunaga et al., 2003), artificial groundwater recharge (Hendrickx et al., 1991), hillslope erosion (Cerdá, 2001; Sauer and Logsdon, 2002), and geotechnical engineering (Zhang and Chen, 2005). Several studies have also addressed the influence that stone fragments have on infiltration and available water content in stony soils. Mehuys et al. (1975) published some of the first research on the effects of rock fragments on unsaturated hydraulic properties and concluded that their presence strongly affects moisture content (θ) and saturated hydraulic conductivity (K_s). Since then, other studies have looked at the influence of stones but have been primarily focused on the determination of saturated parameters (e.g., K_s) or available water content (Cerdá, 2001; Cousin et al., 2003; Hendrickx et al., 1991; Sauer and Logsdon, 2002; Tetegan et al., 2011). Peck and Watson (1979) and Bouwer and Rice (1984) developed pedotransfer functions for determining the unsaturated hydraulic properties of stony soils based on the hydraulic properties of the fine-grained matrix (d < 2 mm) and the proportion of rock fraction (d > 2 mm). Dann et al. (2009) showed that the parameters identified using the fine-grained material, with a correction made for gravel content, can be successfully applied to field-scale studies, but they emphasized the need for in situ studies on bulk material.

Milczarek et al. (2006) and Ma et al. (2010) both focused on estimating unsaturated soil parameters (particularly the curve shape parameters α and n) of coarse materials (sand and gravel) using repacked soil columns while varying the proportion of rock fragments, but they could not determine a clear relationship between the parameter values and the rock fraction. Ma et al. (2010) further suggested that field experiments were essential to provide insight into parameter estimation in stony soils, and other researchers have also suggested that the methods used on soil samples or simulated soil structure are not sufficient to represent field conditions (e.g., Dann et al., 2009; Laloy et al., 2010; Ritter et al., 2003; Wohling and Vrugt, 2011). Numerous studies have been published on obtaining the in situ hydraulic properties of agricultural soils but, to our knowledge, only a few sets of unsaturated hydraulic properties have been published for coarse stony soils (e.g., Milczarek et al., 2006; Ma et al., 2010; Dann et al., 2009), and most have expressed the need for validation from in situ studies. Furthermore, few studies have looked at in situ properties of such coarse conglomeratic soil as that which we considered in this study.

Many of the previous studies involving stony soils were based on either simulated soils or experiments performed on reconstructed soil cores or columns. These methods have been preferred in unconsolidated soils because of difficulties associated with obtaining intact, representative soil samples in coarse alluvial soil. When collecting samples, it is important to capture the heterogeneity of a nonuniform soil, but, because coarse alluvial soils can range in grain size from fine sand or silt to gravel and cobble, representative sample volumes may need to be quite large, which would be logistically difficult to obtain and then perform laboratory tests (Dann et al., 2009; Dunn and Mehuys, 1982; Zhang et al., 2011). Field methods eliminate sampling bias but are difficult in coarse alluvial soils because issues often arise with obtaining proper instrument contact with the soil structure, minimizing disturbance to the soil, and ensuring that sensors are capturing the heterogeneity caused by grain size variation (Cousin et al., 2003; Edwards et al., 1984; Ma et al., 2010). Also, where these soils are poorly consolidated, excavating an open pit face or borehole can be difficult and even hazardous. Despite efforts to characterize the unsaturated hydraulic properties of coarse alluvial soils, there is still a lack of sufficient data to allow general relationships about the hydraulic properties of these soils to be inferred, specifically at field scales (Cousin et al., 2003; Ma et al., 2010), and there have not been sufficient data published to allow property values to be estimated from a literature search or from pedotransfer functions, in contrast to what is available for typical agricultural soils (e.g., Rawls et al., 1982; Carsel and Parrish, 1988; Leij et al., 1996).

In this study, we performed a field-scale infiltration experiment in a heterogeneous, conglomeratic, alluvial sediment sequence that ranged in composition from fine–medium sand to mixed sand and large cobbles (d > 20 cm). Both volumetric soil moisture (θ) and soil tension (ψ [L]) were measured in situ and used to predict the parameters for the van Genuchten–Mualem soil characteristic functions (van Genuchten, 1980). These data were used with a one-dimensional unsaturated flow model (HYDRUS-1D; Šimůnek et al., 2005) combined with a computationally intensive Metropolis–Hastings search method (Metropolis et al., 1953; Hastings, 1970) to optimize the parameters and estimate parameter distributions and correlation. The main purposes of this work were to: (i) quantitatively characterize the unsaturated hydraulic properties of conglomeratic, unconsolidated, alluvial soil in situ based on a field infiltration experiment; (ii) determine whether a soil hydraulic model developed for agricultural soils, the van Genuchten–Mualem (VGM) model, can be used to predict unsaturated behavior in such a soil without explicitly accounting for the influence of gravel and cobbles; and (iii) provide insight into parameter correlation and variance under natural field conditions given limited data.

Experimental Setting

The setting for the infiltration experiment was the Boise Hydrogeophysical Research Site (BHRS) located 15 km southeast of downtown Boise, ID. The site covers 0.036 km^2 of a gravel bar adjacent to the Boise River (Fig. 1). The upper 18 m of the gravel bar consists of coarse, unconsolidated mixed sand, gravel, and cobble deposits with interbedded fine to coarse sand lenses

and underlain by an extensive clay–basalt boundary (Barrash et al., 1999). There is little to no pedogenesis at the site except in low-lying areas upstream from the main well field and along the river edge, where the surface becomes inundated during seasonal flooding. In these areas, surface sediments are primarily sand, gravel, and cobbles but contain a thin surface layer of silt/sand and organic detritus but still no distinct soil horizons. Across the site, the sediment supports vegetation, which includes grasses, shrubs, and deciduous trees, hence our classification of it as an alluvial soil. Vadose zone thickness varies with topography and seasonally with river stage from ~3 m during winter to between 1.5 and 2 m during the summer, when the river stage is higher.

The vadose zone composition is identical to the aquifer composition, which has been extensively studied using numerous hydrologic and geophysical experiments that have identified layered stratigraphy within the aquifer and led to a highly characterized subsurface in terms of saturated properties and material distributions (Barrash and Clemo, 2002; Barrash and Reboulet, 2004; Moret et al., 2006; Dafflon et al., 2011; Bradford et al., 2009; Clement and Barrash, 2006; Clement et al., 2006; Mwenifumbo et al., 2009; Slater et al., 2011). Porosity estimates vary across the site but are generally between 10 and 30% in stratigraphic units identified as mixed sand/gravel/cobble, and up to 50% in sand lenses (Barrash and Clemo, 2002). A number of techniques have been used at the BHRS to estimate K_s, and average values per well or stratigraphic unit range from 0.005 to 1.6 cm s^{-1} (Barrash et al., 2006; Malama et al., 2011; Cardiff et al., 2011, 2012; Straface et al., 2011). More recently, research at the BHRS has been extended into aquifer–atmosphere interactions, including investigations of the evapotranspiration effects on water table drawdown (Malama and Johnson, 2010; Johnson et al., 2013a) and vadose zone hydrology (e.g., this study).

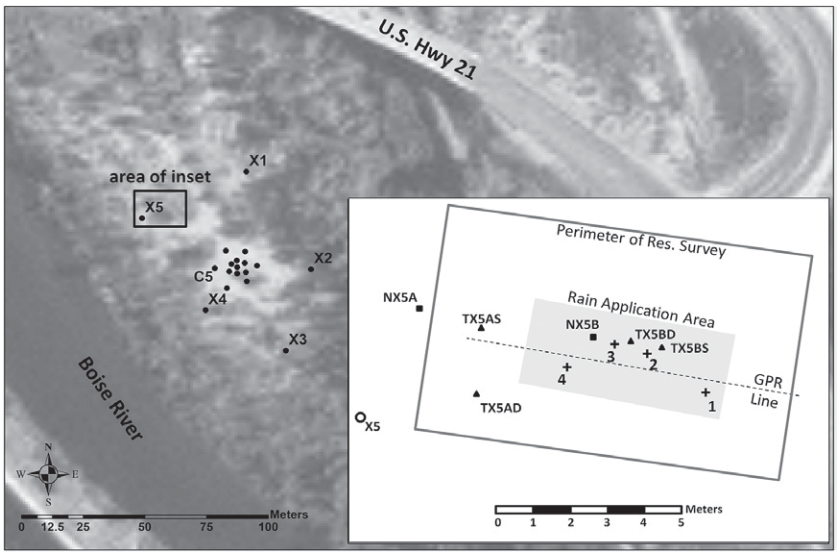

Fig. 1. Areal view of the Boise Hydrogeophysical Research Site showing water monitoring wells and (inset) detailed schematic of infiltration setup showing locations of hydrologic and geophysical measurements (crosses correspond to rain bucket locations).

Tensiometers were used to measure the soil tension (ψ) at the BHRS and were installed as vertically distributed nests using advanced tensiometers (ATs) (Sisson et al., 2002) and a back-fill method well suited to unconsolidated soils that results in very little disturbance of the surrounding material (similar to Hubbell and Sisson [1998] and Cassel and Klute [1986]). Each set was installed as paired shallow and deep nests consisting of four deep (AT1–AT4) and five shallow (AT5–AT9) ATs, with vertical spacing of 0.2 to 0.3 m between sensors. Two of the three tensiometer sets (TX5B shallow and deep and TX5A shallow and deep) were monitored in this study, with TX5B located within the infiltration site and TX5A acting as a control (Fig. 1 inset).

Previous analysis of tensiometer data has shown that the ATs require tension offsets (i.e., constant tension correction that must be applied to each sensor after installation), which are generally <15 cm and are quasi-stable for time periods of weeks to months but can fluctuate by ±5 cm in that same time period (Aishlin et al., 2013). The magnitude and variability of AT offsets are small compared with changes due to natural hydrologic events (e.g., rain, changes in water table elevation, or seasonal drying) or experienced during the test (Aishlin et al., 2013). Uncertainties in AT offsets were later incorporated into the test modeling as instrument errors expressed in the data covariance.

Soil moisture at the BHRS has been measured using a CPN 503DR neutron hydroprobe at several access tubes located across the site. From the summer of 2010 until January 2012, vertical profiles of the entire vadose zone were collected at 2-wk intervals at each of the five access tubes. Moisture data (θ) showed strong seasonal trends of dry soil during hot, dry summer months and wetter soil during cooler, wetter months from fall through spring (Johnson et al., 2013b). Two neutron sites were monitored during the experiment at 1-h intervals: NX5B is located within the infiltration test area and NX5A is nearby to provide a control (Fig. 1 inset).

Preliminary Work

Tensiometer nests TX5BD (deep) and TX5BS (shallow) and neutron access tube NX5B were installed in the spring of 2011 at a location consisting of heterogeneous stratified material. Large-scale structure was interpreted from analysis of high-resolution ground-penetrating radar (GPR) data collected in the summer of 2010, which identified a sand channel aligned east–west with lateral dimensions of approximately 5 by 3 m and thickness ranging from 0.2 to 0.5 m (Fig. 2) and thinning to the southeast. The channel lies between coarser, mixed sand–cobble materials above and below. The TX5BD, TX5BS, and NX5B instrumentation were installed along the long axis of this channel, with

a horizontal spacing of 1 m between each installation (Fig. 1 and 2).

Before installation of TX5BD and TX5BS, soil cores were extracted at these locations. Cores were separated into material samples based on visual composition breaks or, for longer sections where no clear breaks could be identified, into 15.25-cm (6-inch) samples. Core samples were sieved with mesh diameters (d) between 190 and 0.0625 mm (in the method of Reboulet and Barrash, 2003) to develop grain size distributions and to characterize the soil type (Fig. 3). The maximum sampled grain size of these cores was limited by the diameter of the core sample (15.25 cm), but large cobbles (d > 20 cm), which constitute a major portion of the aquifer material, are ubiquitous and underrepresented by this method. Most samples ranged from 50 to 70% (w/w) gravel or cobble (d > 2 mm), with almost no material of silt or finer size (d < 0.0625 mm), and were characterized as mixed sand/gravel. Three samples were dominantly sand; of these, Sections 5S0203 (z = 0.86–0.91 m below land surface [bls]) and 5D0202 (z = 0.73–0.91 m bls) from tensiometer nests TX5BS and TX5BD, respectively, were classified as fine–medium sand (80% < 2 mm) and contained only small amounts of silt (<5%) and gravel (<15%). Section 5S0202 (z = 0.66–0.86 m bls) from TX5BD was classified as coarse sand and contained ~20% gravel. No material similar to 5S0202 was identified in the cores from TX5BD. The depths of these sand samples were all between 0.7 and 1.0 m bls, which corresponds to the depth of the sand channel identified from the GPR data. Similar materials from 5S0203 and 5D0202 were interpreted as a continuation of the same unit, but 5S0202 was interpreted as a local lens, which was confirmed by the GPR data (Fig. 2). Core analysis and stratigraphy from TX5BS were used to determine material distributions for the unsaturated flow model (discussed below).

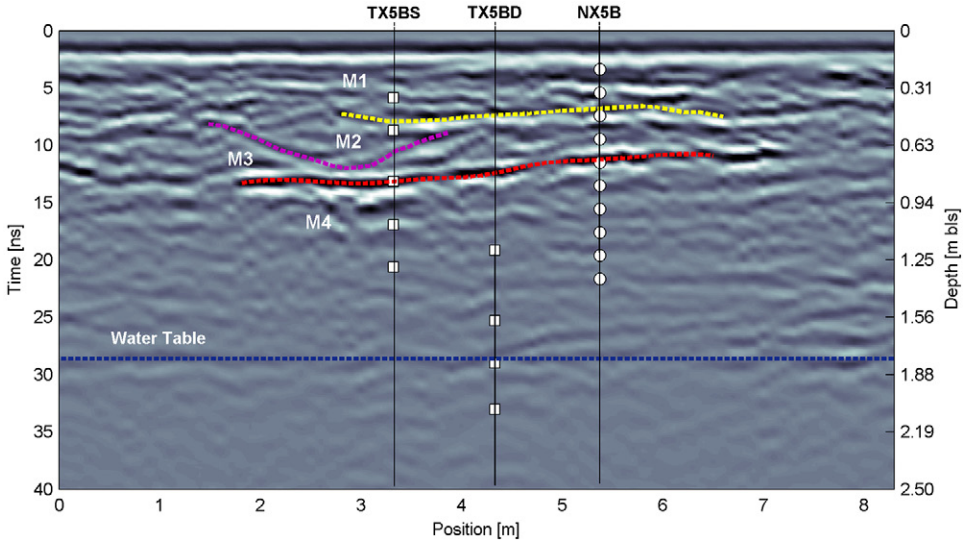

Fig. 2. Two-dimensional ground-penetrating radar survey along long axis of channel showing reflections associated with distinct sediment transitions inferred as a depositional sand channel (dashed lines) and locations of TX5BS and TX5BD tensiometers (squares) and moisture measurements (circles).

Pre-Test Simulation

Before the field experiment, HYDRUS-1D was used to simulate infiltration and provide first-order estimations of the optimal rain application rate (P, cm h^{-1}) and the time required to reach steady state (i.e., continuous flow through the entire vadose zone). The simulation model was set up as a one-dimensional, vertical model consisting of three material layers based on GPR data and soil core analysis: Material 1 (M1), mixed sand and gravel; M2, sand; and M3, mixed sand and gravel. The VGM models were used for θ, ψ, and K relationships:

$$\theta(\psi)=\theta_r+\frac{\theta_s-\theta_r}{\left(1+|\alpha\psi|^n\right)^m} \quad [1]$$

$$K(\theta)=K_s S_e^l\left[1-\left(1-S_e^{1/m}\right)^m\right]^2 \quad [2]$$

where

$$S_e=\frac{\theta(\psi)-\theta_r}{\theta_s-\theta_r} \quad [3]$$

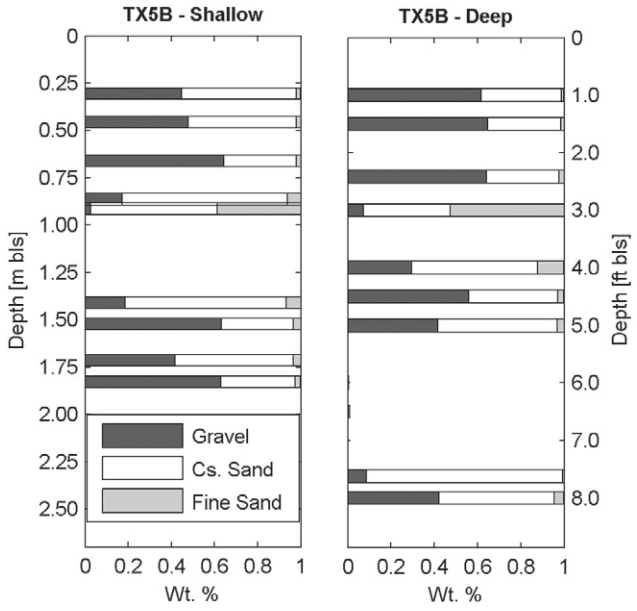

Fig. 3. Grain size classification of TX5B shallow and deep core samples: gravel (>2 mm), coarse sand (>0.25 mm), and fine sand (<0.25 mm). The sand channel is represented in core samples between the 0.75- and 1.00-m depths.

$$m = 1 - 1/n \quad [4]$$

θ_r is the volumetric residual moisture content, θ_s is the volumetric saturated moisture content, α (cm^{-1}) and n (dimensionless) are empirical parameters that are linked to the capillary height and pore size distribution, respectively, but often are treated as shape parameters, K_s ($cm\ s^{-1}$) is the saturated hydraulic conductivity, and l (dimensionless) is related to the soil pore tortuosity but is often given an assumed constant value of 0.5 for most tests (Šimůnek et al., 2005) and is far less sensitive than the other parameters (Abbasi et al., 2003).

The material properties of M1 and M3 for the test simulation were estimated from $\psi(t)$ data collected in TX5A during natural rain events in December 2010 and those of M2 from laboratory infiltration experiments conducted on sand core sample 5D0202 (both methods discussed below). The simulation model was used to aid in test design and to confirm that the desired P would not exceed saturated hydraulic conductivities (i.e., no ponding above any layers) and would reach steady state in an acceptable length of time. These simulations indicated that a rate of P = 1 cm h^{-1} would require ~24 h to reach steady state and would be sufficient to allow continuous flow through the entire vadose zone at rates less than the minimum K_s of any of the layers. This optimal P is much higher than average storms for the Boise area but not uncommon for high-intensity storms, the kind that are more likely to produce flooding and other hazardous conditions, although such storms never exceed a few hours in duration.

Winter 2010 Rain Modeling

In December 2010, several rain events produced observable $\psi(t)$ responses in TX5AS and TX5AD, both of which are near the infiltration test location but outside the wetted perimeter of the experiment. For these events, P averaged ~0.25 cm h^{-1} and storms lasted several hours (Fig. 4). Data from four ATs between 0.47 and 1.92 m bls were used to estimate the unsaturated hydraulic properties of the soil surrounding TX5AS and TX5AD using HYDRUS-1D. Two-dimensional GPR reflection surveys collected for a different purpose near TX5AS and TX5AD show a clear, continuous reflection within the vadose zone, which was inferred to be a material horizon. This led to the use of a two-layer model for simulation of the December 2010 rain response, with both layers interpreted as mixed sand and gravel but with different VGM parameter values allowed for each. The observed tension responses from TX5AS and TX5AD (Fig. 4) were used to optimize the parameters using Monte Carlo sampling along with trial-and-error adjustments. The root mean squared error between the observed and simulated $\psi(t)$ was used to determine the optimal parameter values, which are shown in Table 1. Final optimal values were within the range expected for sandy soils (for parameters α and n) and BHRS sediments (for parameters θ_s and K_s). In-depth statistical analysis of the soil parameters was not performed for these data because the goal of this modeling was to quickly provide initial estimates of vadose zone properties at the BHRS for use in the pre-test simulations.

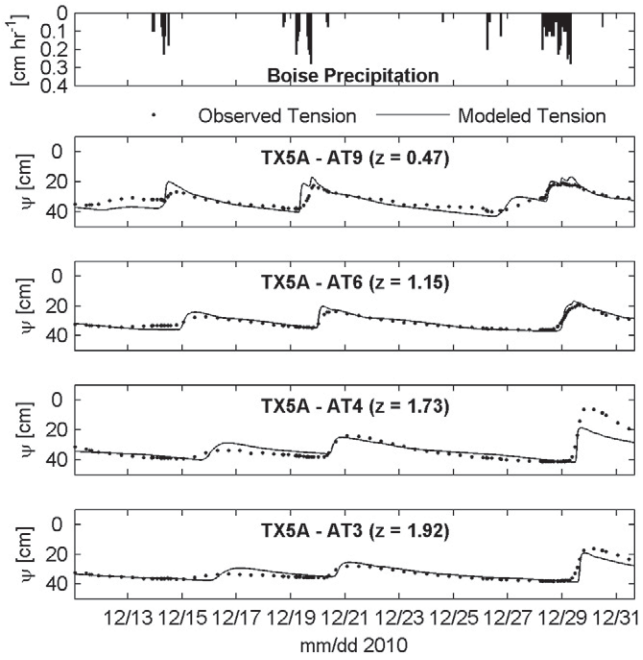

Fig. 4. Results of modeling the winter 2010 rain events measured by tensiometer set TX5A, showing observed and predicted tension (ψ) responses to several rain events.

Sand Core Properties

The high-resolution GPR reflection surveys conducted over the infiltration site indicated that the fine–medium sand zone did not extend into the area of TX5AD where the December 2010 rain responses were modeled. Correct simulation of the infiltration experiment thus required inclusion of the effects of this distinctly different material. To obtain an initial estimate of the parameters, the fine–medium sand core sample (5D0203) was repacked into a 5.08-cm i.d. clear polyvinyl chloride tube, compacted to a length of 16 cm to achieve approximately the same volume as the original core sample, and placed under an array of greenhouse misters. The top of the core was left open and the bottom was supported with a fine mesh screen. Water was applied

Table 1. Optimal van Genuchten–Mualem volumetric saturated soil moisture (θ_s), saturated hydraulic conductivity (K_s) and shape parameters α and n from both the winter 2010 rain modeling and core laboratory tests.

Material	Method	θ_s	α	n	K_s
			cm^{-1}		$cm\ s^{-1}$
Material 1	winter 2010 rain response	0.31	0.22	2.46	0.239
Material 2	winter 2010 rain response	0.27	0.22	1.72	0.150
5D0203	core laboratory test	0.33	0.30	2.96	0.0045

to the top of the tube at a rate of $P = 5.0$ cm h^{-1} for ~1 h, and the times when the wetting front arrived at five chosen vertical locations along the length of the tube were measured. The initial θ was assumed to be near zero for the oven-dried sample, and final θ was determined by the weight of the wet soil column minus the dry sample weight (final θ ≈ 0.36). Core porosity was estimated from the volume of the dry material (assuming a material density of 2.6 g cm^{-3} for quartz sand) divided by the volume of the intact core. The estimated porosity was 0.41, which is within the range of porosity estimates of BHRS sand zones (Barrash and Clemo, 2002).

Parameter values for the core material were initially determined using the Rosetta Neural Network Prediction module built into HYDRUS-1D with inputs of sand, silt, and clay contents (85, 15, 0%, respectively) and a bulk density of 1.45 g cm^{-3} as measured from the sample dry weight divided by the core volume. The θ_s value (i.e., the effective porosity) predicted from Rosetta was within 0.01 of the estimated porosity (0.41), and parameter values predicted by Rosetta were used in HYDRUS-1D to simulate the wetting front propagation along the column. The model top boundary was set as a specified flux equal to 5.0 cm h^{-1}, and a free drainage boundary was prescribed at the bottom. The model-predicted times when the wetting front passed five locations (t_{wf}) were compared with the actual times measured in the laboratory. The calculated t_{wf} using the Rosetta-predicted values were all within 4 min of the observed t_{wf} at all measurement locations (Fig. 5), with a correlation coefficient (R^2) of 0.98. These Rosetta-predicted parameter values (Table 1), although representing properties of a reconstructed core and not in situ properties, were used in the pre-test simulation and also to provide a starting point for optimization of the infiltration test. As with the December 2010 modeling, an extensive analysis of the parameters was not performed because it was not the focus of this experiment.

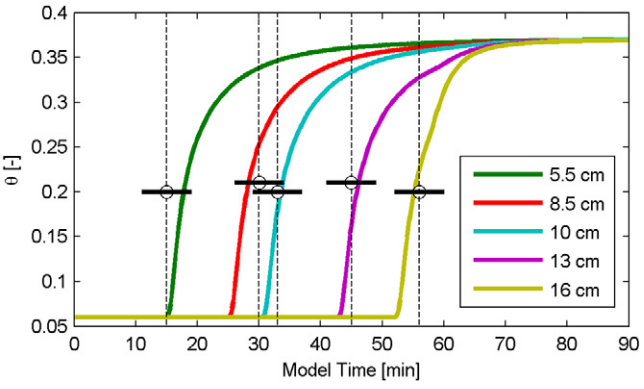

Fig. 5. Calculated wetting curves at observation nodes (solid lines) and observed wetting front times (circles and vertical dashed lines) from the sand core rain test performed on core sample 5D0203. Legend shows depths of wetting front passage measurement locations; tick bands on circles show ±4 min error.

Field Infiltration Experiment Setup

A 5- by 2-m area surrounding installations TX5BS, TX5BD, and NX5B was used for the infiltration test (see Fig. 1 inset); these dimensions allowed wetting to surround the area of all three installations by ≥1 m. During the experiment, the infiltration site was covered with waterproof canopies and surrounded with waterproof tarps to minimize the effects of evaporation and wind redistribution. Water was applied using 66 Agrifirm 0.5 GPH Turbo-Flo mist nozzles placed 1.5 m above the land surface in a staggered grid pattern (0.5 m between misters on a single row and 0.35 m between rows) to provide optimal coverage. There are several advantages to using these mist nozzles rather than more conventional sprinklers or drip lines: (i) the small droplet size minimizes impact effects; (ii) they can be placed at any height above the land surface, which allows access beneath the misters and direct measurements of P at the soil surface; (iii) the application rate can be easily adjusted by changing either the incoming water pressure, the nozzle height above the ground, or the nozzle spacing; (iv) nozzles are interchangeable and available with different flow rates, allowing a further range of application rate; and (v) they are inexpensive and can be obtained from most irrigation supply distributers. The precipitation rate was measured using four tipping buckets, calibrated before and after the experiment, placed on the land surface within the application area and connected to a Campbell Scientific CR1000 datalogger. Water supplied to the misters was extracted from Well C6, which is 35 m from the infiltration site. With the low pumping rate (<19 L h^{-1}), fully screened well, and high-K_s aquifer, water table drawdown (Δwt) near the infiltration site caused by pumping was not measurable (Δwt < 0.31 cm) during the test.

The infiltration experiment began on the morning of 1 Aug. 2011 at 1130 h. Campbell Scientific CR1000 dataloggers were used to record ψ in tensiometer sets TX5A and TX5B with a measurement frequency of 3 min, and full vertical θ profiles were collected every 1 h in NX5A and NX5B. The NX5A site and TX5A set (consisting of nests TX5AS and TX5AD) were outside the infiltration area but within 2 m of the perimeter and were monitored to observe background changes in θ and ψ and to confirm that water was not migrating laterally beyond the application area. Water table depth was measured in Well X5 (<4 m from the infiltration area) at 4-h intervals and showed no change throughout the experiment. Tensiometer data were output in real time to laptops set up in a tent adjacent to the test area to monitor progress. After ~19 h, it was decided that vertical ψ and θ profiles had reached steady state under wet conditions (pre-test simulations predicted ~24 h), and after waiting another 4 h, the misters were turned off on 2 Aug. 2011 at 0721 h. For approximately 11 h after turning off the misters, all measurements were recorded at the same time intervals and by the evening of 3 Aug. 2011, much of the equipment was removed and θ measurements were expanded to two to three times

per day until 5 Aug. 2011. Measurements of ψ continued at 3-min intervals until 5 Aug. 2011. Long-term ψ and θ data later showed that soil moisture did not return to pre-test values until >1 wk after rain application ceased.

In addition to hydrologic measurements, two-dimensional, multi-offset GPR reflection and three-dimensional dipole–dipole electrical resistivity surveys were collected every hour during the infiltration experiment from 1 through 3 Aug. 2011. The GPR surveys were collected along the main transect of the installations using shielded antennas, and the ends of this transect extended beyond the wetted area. The resistivity survey also extended beyond the wetted perimeter to delimit the wetted perimeter and to observe lateral moisture migration, if any. Initial review of the resistivity and GPR data, along with tension measurements in set TX5A and moisture measurements in NX5A (not shown), confirmed that there was no observable lateral migration of water outside the application area.

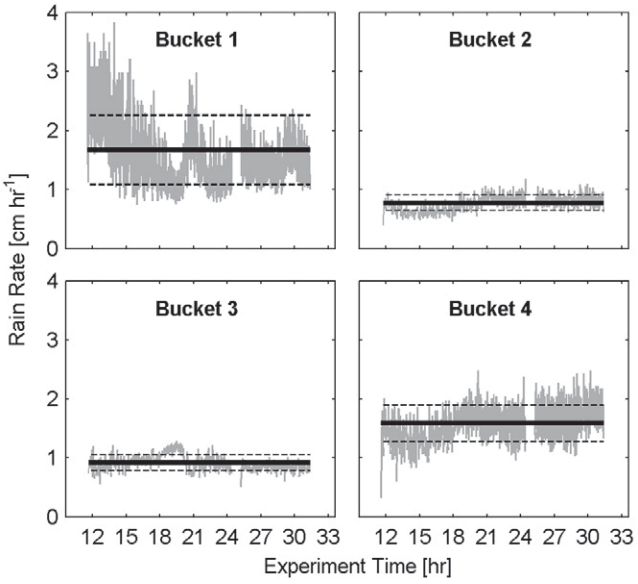

Fig. 6. Rain application rate from the four rain buckets; solid lines are mean values and dashed lines are ±σ.

Infiltration Test Results

The four rain buckets recorded recognizably different *P* values within the experiment boundary (Fig. 6). Buckets 1 and 4 showed mean *P* values of 1.67 and 1.59 cm h^{-1}, respectively, with standard deviations (σ) of 0.31 and 0.59 cm h^{-1}, while Buckets 2 and 3 (the two buckets closest to TX5BS, TX5BD, and NX5B) showed considerably less noise in the measurements (σ < 0.14 cm h^{-1} for both) and mean *P* values of 0.77 and 0.92 cm h^{-1}, respectively. Higher σ values from Buckets 1 and 4 were probably the result of the buckets being jostled or becoming tilted during the experiment, as they were located closer to the edge of the application plot where there was considerable foot traffic related to geophysical data collection and other logistics. For that reason, we used a constant *P* of 0.84 cm h^{-1} (2.3 × 10^{-4} cm s^{-1}) determined from the mean of Buckets 2 and 3 as the upper boundary flux in the infiltration model because these two buckets were located closest the measurement locations. Note that this precipitation rate is far less than the previously estimated K_s of any of the materials (Table 1) but still much greater than natural precipitation rates and durations (e.g., events described for winter 2011 modeling above). This was an essential part of the experiment to avoid oversaturation of sediments and ensure continuous flow through all layers.

Measurements of θ were taken in NX5B and NX5A from 0.15 m bls to just above the water table (~1.5 m bls) with vertical spacing of 0.15 m (0.5 ft). Four θ(*z*) and ψ(*z*) profiles from selected times during the experiment are shown in Fig. 7. Figure 7A shows initial θ(*z*) and ψ(*z*) profiles and Fig. 7D shows the first measurements after steady state was reached and before ending the rain application. Long-term ψ(*t*) and θ(*t*) data from the beginning of the experiment until several days after are shown together in Fig. 8 for different tensiometer depths and comparable θ measurement depths (vertical differences between ψ and θ measurements in Fig. 8 are <20 cm). Raw ψ(*t*) data before and during the arrival of the wetting front had a σ of ~2 cm for all tensiometers, but ψ(*t*) data after steady state had been reached

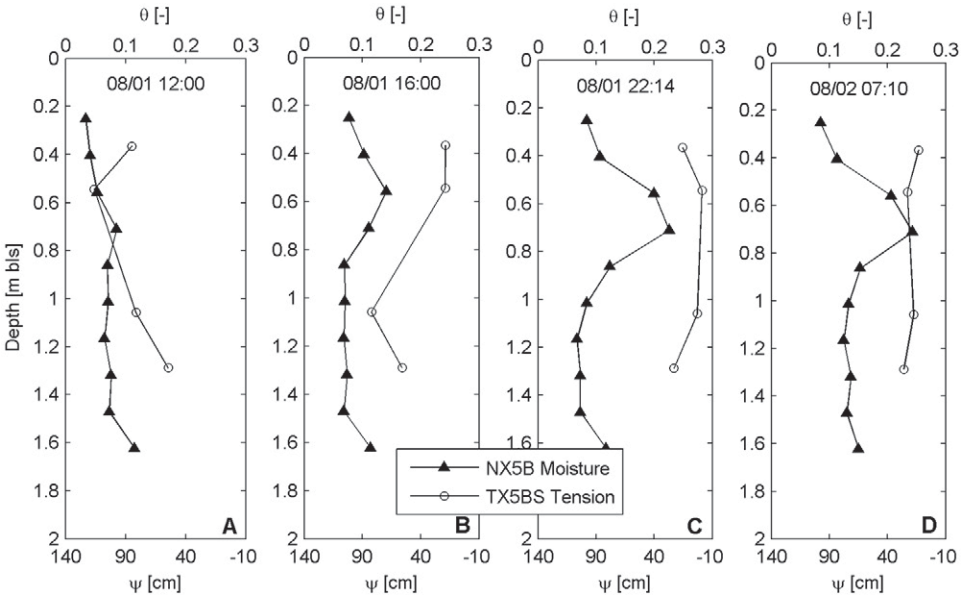

Fig. 7. Soil moisture θ(*z*) and tension ψ(*z*) profiles at select times during the experiment: (A) initial profiles, (B,C) during the test, and (D) steady state.

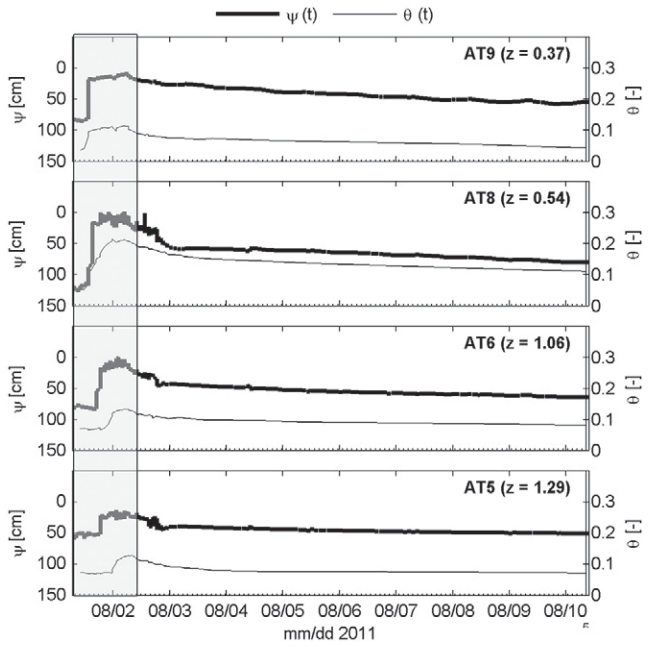

Fig. 8. Observed tension $\psi(t)$ and moisture $\theta(t)$ data from the beginning of the experiment to 10 d after. Moisture data presented are from measurement depths nearest to advanced tensiometer (AT) depths in neutron site NX5B. Shaded region denotes modeling focus time.

became noisier and σ values increased to 12 to 14 cm for all tensiometers except AT7 and AT9. All $\psi(t)$ data were processed by averaging each data point with the previous and following points (three measurements or a 9-min window) to reduce noise. This averaging reduced σ for the $\psi(t)$ data to near 2 cm for all tensiometers but did not significantly affect the timing of the arrival of the wetting front or the shape of the transient portions of the $\psi(t)$ curves. The ψ(t) measurements at AT7 are not included in the results or in the modeling due to questionable behavior before the start of the experiment, probably related to a damaged AT sensor or housing.

Comparison of wetting front arrival times between $\psi(t)$ and $\theta(t)$ shows that there was a significant delay (~6 h) in the $\theta(t)$ response at the depths of sensors AT6 and AT5 compared with the $\psi(t)$ response (Fig. 8), which is much more of a delay than would be expected by differences in depths between the two sets of measurements (<20 cm). Although not shown, $\psi(t)$ data recorded by AT4, located slightly above AT5 but 1 m closer to NX5B (see Fig. 2), were also delayed in arrival of the wetting front compared with AT5 by ~3.6 h. We suspect that the progressively greater delay was due to lateral variation in Material M3 thickness between TX5BS and NX5B (see Fig. 2) because AT6, AT5, and the corresponding θ measurements are located below the fine–medium sand layer observed from core samples and GPR data. The GPR data along with core samples from TX5BS and TX5BD showed that the fine–medium sand section is 7 to 12 cm thicker at TX5BD than at TX5BS and that the medium–coarse sand section (5S0202) is completely absent at the location of NX5B. The variable thickness of the fine–medium sand zone between TX5BS and NX5B combined with the lower K_s of this material (see Table 1) were probably causing the delay in wetting front propagation between TX5BS and NX5B. The significant difference in the response time between ψ and θ data at similar depths excludes the use of simpler methods of optimizing the VGM parameters through direct fitting of the observed $\theta(\psi)$ data as other studies have done (e.g., Vrugt et al., 2003a; Milczarek et al., 2006).

Infiltration Test Model

Albeit with recognition of the apparent lateral heterogeneity just described, we modeled the infiltration experiment over TX5BS using the HYDRUS-1D model as a first approximation and base case to compare with more detailed modeling to follow (which will include two-dimensional distribution of materials and geophysical data). Because the heterogeneity limits the use of simultaneous ψ and θ data in a one-dimensional model to optimize parameters, we focused on fitting $\psi(t)$ data from TX5BS and include only an initial θ measurement (before the start of the test: θ_{dry}) and final θ measurement (after the wetting front had passed and steady-state flow had been reached: θ_{wet}) for three θ measurement depths corresponding to separate material layers. Tension data were chosen as the primary data to fit because they provided a sharper transition from dry to wet conditions and thus a better representation of the wetting front arrival than the moisture data, and tension data errors are smaller relative to the total change in tension than moisture data. Including θ_{wet} and θ_{dry} was done to achieve a better representation of the soil properties because it forced the model to find curves that pass through $\theta(\psi)$ points of the initial and steady-state observations, thus providing further constraint. In this regard, Zou et al. (2001) have shown that including only initial and final moisture measurements in wetting experiments can increase parameter predictability.

Material distributions for the infiltration test model were similar to the pre-test simulation model except that the infiltration test model was separated into four material layers instead of three; in addition to a fine–medium sand layer, the infiltration model included a coarse sand with gravel layer represented by core sample 5S0202 (Fig. 9). The model geometry extended from the land surface (z = 0 cm) to z = −300 cm, with material contact depths determined from GPR data and core samples (Fig. 2 and 3). Both M1 and M4 represent coarse, poorly sorted, mixed sand/gravel/cobble, M2 represents medium–coarse sand with gravel (e.g., core section 5S0202), and M3 represents a uniform medium–fine sand (core section 5S0203). The model was discretized with elements ranging in thickness from 0.54 to 5.4 cm and with finer discretization around M3. Initial model time (t_0) was 1 Aug. 2011, 0000 h, and the model was run for 24 h, which was an adequate time to reach steady state. Time step

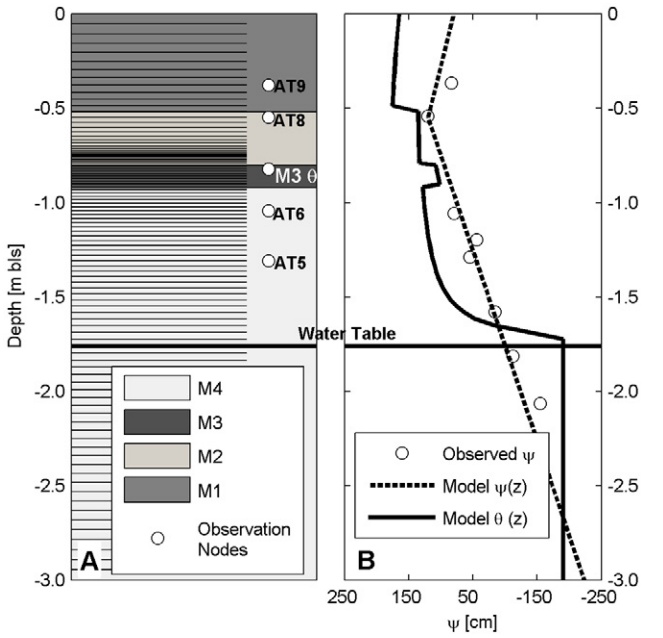

Fig. 9. (A) HYDRUS-1D model setup showing distribution of materials M1 to M4, grid discretization, and locations of tensiometer (AT) and moisture measurement nodes; (B) initial model tension (ψ) and moisture (θ) profiles and initial observed ψ data (circles) prior to test.

discretization is internal to HYDRUS-1D software and is continuously adjusted to achieve convergence (Šimůnek et al., 2005). Final mass balance errors were, on average, <3% for all model runs.

The initial conditions of the model were set, using the observed water table depth as $\psi = 0$ cm at $z = -176$ cm and measurements from the tensiometers immediately before the experiment to calculate a $\psi(z)$ relationship from the water table to the land surface. Observed ψ increased (decreasing negative pressure) above the water table to the depth of AT8 (−55 cm), then decreased slightly between AT8 and AT9. Below the water table, $\psi(z)$ was set to a 1:1 function, with increasing positive pressure equal to hydrostatic pressure. Initial $\theta(z)$ values were set automatically based on the initial VGM parameters for the four different materials and the initial tension profile. Observation nodes were placed at depths corresponding to AT9, AT8, AT6, and AT5, with an additional observation node placed within Material M3 to track θ in that material. Two nodes used for AT9 and AT5 where used to track θ in M1 and M4.

The upper model boundary was set as a variable flux boundary with $P = 0.84$ cm h^{-1} (mean of Buckets 2 and 3) for the time of rain application (from 11.6 h [model time] to 24 h) and $P = 0$ cm h^{-1} otherwise. The lower boundary was set as a head-dependent flux boundary, with a critical head value of 124 cm (the height of the water table above the base of the model). This condition maintains a constant water table depth and represents water being dispersed laterally on reaching the saturated zone (i.e., no recognizable mounding).

Metropolis–Hastings Optimization

Optimization of the VGM parameters was achieved using five independent Metropolis-Hastings (MH) sampling algorithms, with five separate initial parameter sets, each run to 10^6 samples. The MH algorithm was similar to the method described by Cardiff et al. (2011) (below we provide a brief description of the process but refer the reader to Cardiff et al. [2011] for further details). The MH algorithm is a Markov chain Monte Carlo (MCMC) type method that seeks to generate a set of samples (the Markov chain) that is representative of the model parameters' posterior probability density. The MCMC methods are advantageous for modeling in the vadose zone because models of vadose zone behavior (i.e., Richards' equation and VGM relationships) are strongly nonlinear and parameters are often highly correlated, which can complicate gradient-based optimization methods (Vrugt et al., 2003b; Vrugt and Bouten, 2002). The MH algorithm incorporates a downward-stepping function that takes a step from an initial position in a random direction (guided by parameter covariance) and always accepts parameter sets that produce a higher likelihood (better fits to the data) but also accepts parameter sets of lower likelihood with a certain probability (i.e., occasionally accepts parameters that produce a worse fit to the data). The former ensures that "peaks" of the parameters' posterior probability are discovered, while the latter allows the algorithm to explore the full parameter space and rigorously estimate parameter uncertainty. In the case of symmetric jump distributions (this study), the MH algorithm reduces to the Metropolis algorithm but we maintain the use of the MH abbreviation for the purpose of consistency with previous uses of this algorithm (e.g., Cardiff et al., 2011). The algorithm used in this study is similar to the one used by Cardiff et al. (2011) for estimating saturated hydraulic parameters of the BHRS aquifer, and minor adjustments were made to the code to incorporate the needs of the current model (e.g., check for bounds, check forward model nonconvergence, etc.). We used the MH algorithm rather than recently developed shuffling algorithms (Vrugt et al., 2003a) because, despite the advancements made by these methods, the MH algorithm is a widely accepted method that is statistically sound, easy to implement, readily available, and can easily be run on multiple computers without the use of parallel computing strategies.

The MH algorithm explores the parameter likelihood, or equivalently, the negative log likelihood (NLL) function

$$\mathrm{NLL} = \frac{1}{2}\left(\mathbf{d}_{\mathrm{err}}^{\mathrm{T}}\mathbf{C}_{\mathrm{d}}^{-1}\mathbf{d}_{\mathrm{err}}\right) \quad [5]$$

where $\mathbf{d}_{\mathrm{err}}$ is a vector of the error between the observed and calculated data [for both $\psi(t)$ and $\theta(t)$] and $\mathbf{C}_{\mathrm{d}}$ is the data covariance matrix, a diagonal matrix with elements equal to the estimated error, or variance (σ^2), of the data. For tension data, the observed σ_{ψ} was only 2 cm, but this incorporates measurement error only. Given the additional uncertainty in AT depths and material

depths, as well as AT offsets mentioned above, σ_ψ for $\mathbf{C}_d$ was increased to 8 cm to incorporate all errors. For θ measurements, the observed σ_θ was 0.03 based on instrument precision (Johnson et al., 2013b), but we used a value of twice this amount in $\mathbf{C}_d$ to account for the influence of uncertainty in measurement depth and sampling volume on the neutron moisture data. The $\mathbf{d}_{err}$ vector included ~100 data points (300 min) for each of the four ATs in TX5BS, with the data centered on the times when the wetting front passed each sensor as well as θ_{dry} and θ_{wet} for each of three materials: M1, M3, and M4 (observation nodes AT9, M3θ, and AT5, respectively, in Fig. 9). Selection of $\psi(t)$ data in this manner eliminated large amounts of redundant and nontransient data in the optimization. The choice of θ_{dry} and θ_{wet} was described above.

The VGM parameters θ_s, α, n, and K_s were optimized for each of the four materials. The value of θ_r was fixed for each of the material layers based on the measured moisture content before the test (0.03–0.05 for all materials) because θ_r has been shown to have low identifiability in similar modeling experiments (Scharnagl et al., 2011; Inoue et al., 1998; Šimůnek et al., 1998). The starting point (initial parameter set) for the MH sampling was obtained from the results of a direct search (DS) optimization using the MATLAB *fminsearch* function. Direct search methods were suggested by Liu et al. (2010) to be done before MH methods to provide a better starting position. Initial values for the DS optimization were obtained from the winter 2010 rain modeling for M1 and M4 and the results of the laboratory core experiment for M3. The M2 initial α and n values for the DS method were prescribed to that of M3 (similar relatively fine material), and θ_s and K_s were set to values typical of BHRS sand layers (Barrash and Clemo, 2002; Barrash et al., 2006). The DS optimization reduced the NLL from an initial value of 465 to 223. While the DS method did not provide very good fits to the observed $\psi(t)$ and θ data, the results did provide a better initial state for the MH sampling.

The robustness of MH methods comes from the use of a large number of iterations to explore the parameter space, which makes MH algorithms computationally intense and time consuming. The larger the number of iterations (e.g., $t \rightarrow \infty$), the more likely the algorithm is to find the optimal parameter set and the better it will predict parameter variances (σ^2) and joint probability density functions. Liu et al. (2010) and others discussed how the results from a single MH chain are often insufficient in identifying the optimal parameters and estimating the variance and suggested that multiple chains, starting from different initial parameter sets, are better at searching the entire parameter space and achieving convergence.

The first MH chain (MH_1) was started with the initial parameter set taken from the results of the DS optimization mentioned above. For the remaining chains (MH_2–MH_5), the initial sets were chosen by picking four parameter sets from within uniform distributions, within reasonable bounds, such that the calculated initial NLL of the chosen set (Table 2) was <1.5 times the NLL of the DS results.

The size of the steps taken between successive samples in the MH algorithm, or search radius, is determined by the parameter covariance matrix ($\mathbf{C}_m$), which is a measure of the local σ^2 of each parameter and the covariance between parameters (Tarantola, 2005). The $\mathbf{C}_m$ matrix is then multiplied by a standard normal distribution and the resulting vector is added to the current parameter set to produce the next set. Parameters that have larger σ^2 will allow the MH sampler to take larger steps in that direction, which will more quickly explore the parameter space of less resolved parameters. The $\mathbf{C}_m$ matrix was estimated from

$$\mathbf{C}_m = \left(\mathbf{J}^T \mathbf{C}_d \mathbf{J}\right)^{-1} \quad [6]$$

Table 2. Initial volumetric saturated soil moisture (θ_s), saturated hydraulic conductivity (K_s) and shape parameters α and n used in all five Metropolis–Hastings (MH) sampling runs and lower and upper bounds.

Material	Run	θ_s	α	n	K_s
			cm^{-1}		$cm\ s^{-1}$
M1 (sand and gravel)	MH_1	0.31	0.22	2.46	0.239
	MH_2	0.23	0.32	2.57	0.064
	MH_3	0.20	0.24	3.54	0.018
	MH_4	0.34	0.27	1.66	0.312
	MH_5	0.23	0.16	1.79	0.108
	bounds	0.15–0.35	0.04–0.5	1.0–4.0	0.002– 0.6
M2 (coarse sand and gravel)	MH_1	0.15	0.22	3.29	0.055
	MH_2	0.15	0.28	2.49	0.250
	MH_3	0.14	0.46	1.55	0.058
	MH_4	0.14	0.28	1.51	0.493
	MH_5	0.12	0.40	1.87	0.240
	bounds	0.10–0.40	0.04–0.5	1.0–4.0	0.002–0.6
M3 (uniform fine–medium sand)	MH_1	0.33	0.30	2.96	0.0045
	MH_2	0.37	0.12	1.38	0.044
	MH_3	0.44	0.16	3.96	0.0086
	MH_4	0.48	0.27	1.50	0.067
	MH_5	0.35	0.15	1.66	0.0033
	Bounds	0.20–0.50	0.04–0.5	1.0–4.0	0.0003–0.6
M4 (sand and gravel)	MH_1	0.27	0.22	1.72	0.150
	MH_2	0.19	0.25	3.24	0.089
	MH_3	0.20	0.13	3.09	0.294
	MH_4	0.30	0.26	3.51	0.240
	MH_5	0.35	0.13	3.55	0.246
	bounds	0.15–0.35	0.04–0.5	1.0–4.0	0.002–0.6

where **J** is the numerical finite-difference Jacobian matrix evaluated at the current parameter set and $\mathbf{C}_d$ is the data covariance matrix as in Eq. [5]. In the five separate MH chains, $\mathbf{C}_m$ was updated every 10^5 iterations using the latest parameter set to ensure a more efficient search of the parameter space as the MH algorithm evolved. From 5×10^5 through 1×10^6 samples, the $\mathbf{C}_m$ matrix did not change considerably.

Prior information can be incorporated into the MH algorithm by several methods (Liu et al., 2010), but given the nature of the infiltration experiment and associated information, we chose to enforce bounds to all parameters (Table 2) based on what has been observed at the BHRS for saturated parameters θ_s and K_s or what is likely for coarse materials for unsaturated parameters α and n. Any parameter set that had >0 parameters outside these bounds returned an NLL well above the values expected from in-range parameters. The average number of out-of-bound samples for the five separate chains was between 45 and 65%.

Potential Scale Reduction Factor

A scale reduction (SR) factor is used as an unbiased assessment of whether multiple MH chains have converged on a single distribution (Gelman and Rubin, 1992):

$$\mathrm{SR} = \sqrt{\frac{1-g}{g} + \frac{q+1}{q}\frac{B}{W}} \qquad [7]$$

where g is the number of samples used, q is the number of independent chains, W is the mean of all σ values from each independent chain, and B is the variance of all μ values from each individual chain. The SR should reduce with evolution of the chains as each chain samples through the parameter space and the statistical aspects of individual chains become similar to the aspects of all chains combined (Liu et al., 2010). If multiple chains converge to the same parameter space with similar statistical properties, SR will approach 1 and the chains and full model are said to have converged, but, because this is unlikely with uncertainty in the data, Gelman and Rubin (1992) suggested that a value of 1.2 is sufficient to declare convergence. We calculated SR with all five MH chains beginning at step 5×10^5 and continuing to step 1×10^6 and discuss the results below.

Metropolis–Hastings Results and Parameter Distributions

Probability distributions for each parameter from each of the five MH chains are shown in Fig. 10 along with the distributions from the set of all five chains combined ($\mathrm{MH}_{\mathrm{all}}$). Parameter mode (Mo) and standard deviation (σ) values from $\mathrm{MH}_{\mathrm{all}}$ are presented in Table 3 along with the calculated final SR (after 1×10^6 samples). These calculations and distributions disregard the first 5×10^5 samples as a "burn-in" period. The final SR for 11 of the 16 parameters was <1.2, implying agreement between chains for several individual parameters but not convergence of the full model. The SR values tracked through the last few thousand samples showed little signs of reduction, and mode (Mo) values for those parameters with SR > 1.2 also showed little to no change. We infer from the invariability of the SR and Mo values for specific parameters that full model convergence could not be obtained within a reasonable number of steps and this perhaps expresses the limitations of the current model (discussed below).

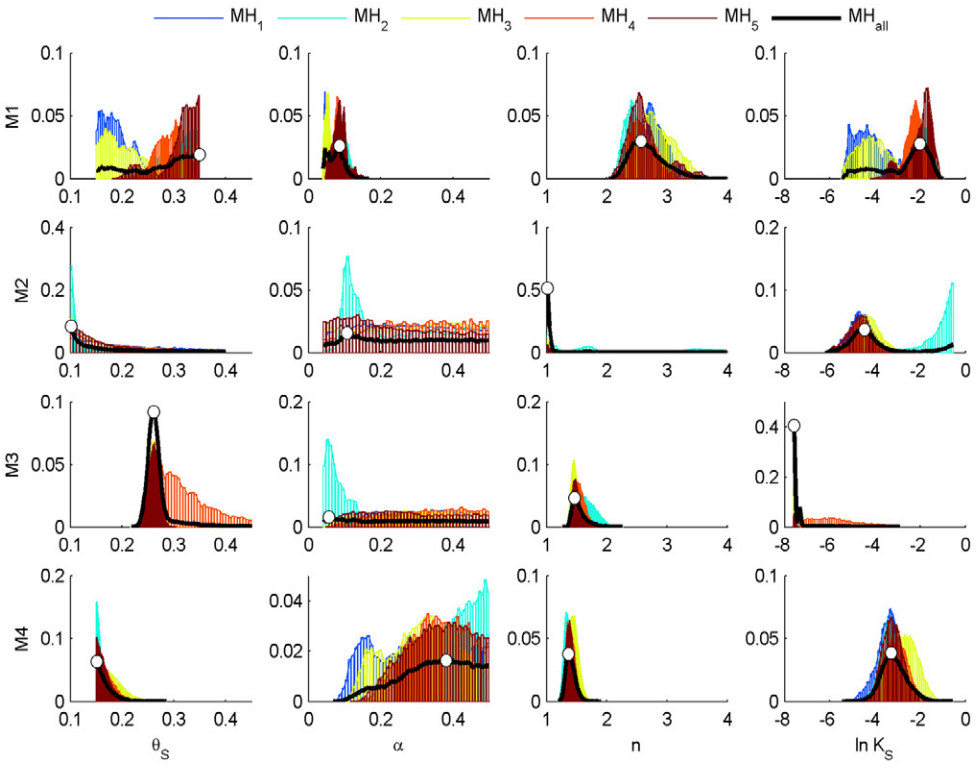

Fig. 10. Cumulative distributions of saturated moisture content (θ_s), curve shape parameters α and n, and saturated hydraulic conductivity (K_s) from all five independent Metropolis–Hastings (MH) chains and all chains combined (black lines) for materials M1 to M4. White circles are mean values from combined chains.

Table 3. Mode (Mo) and variances (σ) of volumetric saturated soil moisture (θ_s), saturated hydraulic conductivity (K_s), and shape parameters α and n from the combined distribution of all five Metropolis–Hastings chains and scale reduction (SR) after 1×10^6 samples.

Material	Parameter	θ_s	α	n	K_s
			cm^{-1}		$cm\ s^{-1}$
M1 (sand and gravel)	Mo_{all}	0.349	0.085	2.567	0.133
	σ_{all}	0.060	0.021	0.285	0.074
	SR	1.58	1.55	1.11	1.67
M2 (coarse sand and gravel)	Mo_{all}	0.102	0.107	1.016	0.012
	σ_{all}	0.076	0.132	0.649	0.139
	SR	1.03	1.02	1.07	1.03
M3 (uniform fine–medium sand)	Mo_{all}	0.261	0.056	1.468	5×10^{-4}
	σ_{all}	0.037	0.136	0.125	0.004
	SR	1.44	1.02	1.07	2.12
M4 (sand and gravel)	Mo_{all}	0.151	0.381	1.366	0.038
	σ_{all}	0.017	0.096	0.080	0.034
	SR	1.08	1.06	1.10	1.16

Initial NLL values from the five independent chains were: 223, 256, 232, 232, and 279; after the first 3×10^5 samples, however, NLL was reduced to <45 for all chains and remained primarily between 15 and 35 for the remaining steps (Fig. 11). The consistent range of NLL values within each chain and similar values between chains after the burn-in suggest that all MH chains reached an optimal minimum NLL region that could not be reduced further.

Important observations about the resolution of the parameters and the sensitivity of the experiment and forward model to the parameters can be made from the parameter distributions in Fig. 10 and σ values in Table 3.

1. Several parameters appear to have converged to distributions that were near normal with clearly identifiable Mo values ($\theta_{s,M3}$, n_{M1}, n_{M3}, n_{M4}, $K_{s,M2}$, $K_{s,M4}$), implying agreement between chains and a high resolution of those parameters with clear optimal values.
2. Distributions for $\theta_{s,M1}$, $K_{s,M1}$, and α_{M4} show little agreement between individual chains (little overlap), leading to wide distributions (high σ) for MH_{all}, which is quantified by SR > 1.5 for all three parameters and indicates non-uniqueness.
3. Some distributions ($\theta_{s,M2}$, $\theta_{s,M4}$, $K_{s,M3}$) were strongly affected by the bounding values, which implies that optimal values may be outside the bounds (i.e., $\theta_s < 0.15$), which, as described above, were based on saturated tests performed in this region of the aquifer. As we discuss below, this is probably related to the resolution of the parameters and the sensitivity of the model to those parameters.
4. Parameters α_{M2}, α_{M3}, and α_{M4} each appear to converge to a single distribution, but these distributions were nearly uniform and are thus uninformative, implying that those parameters have little influence over the model and data fit. Similarly, the fact that σ values are more than four times greater for n_{M2}, n_{M3}, and n_{M4} than n_{M1} (Table 3) implies that the model is most sensitive to n_{M1}.

A more detailed discussion of the potential causes and implications of these observations is made below.

Parameter Covariance and Correlation

It is widely understood that VGM parameters are often highly correlated, and cross-correlation, which contributes to non-uniqueness,

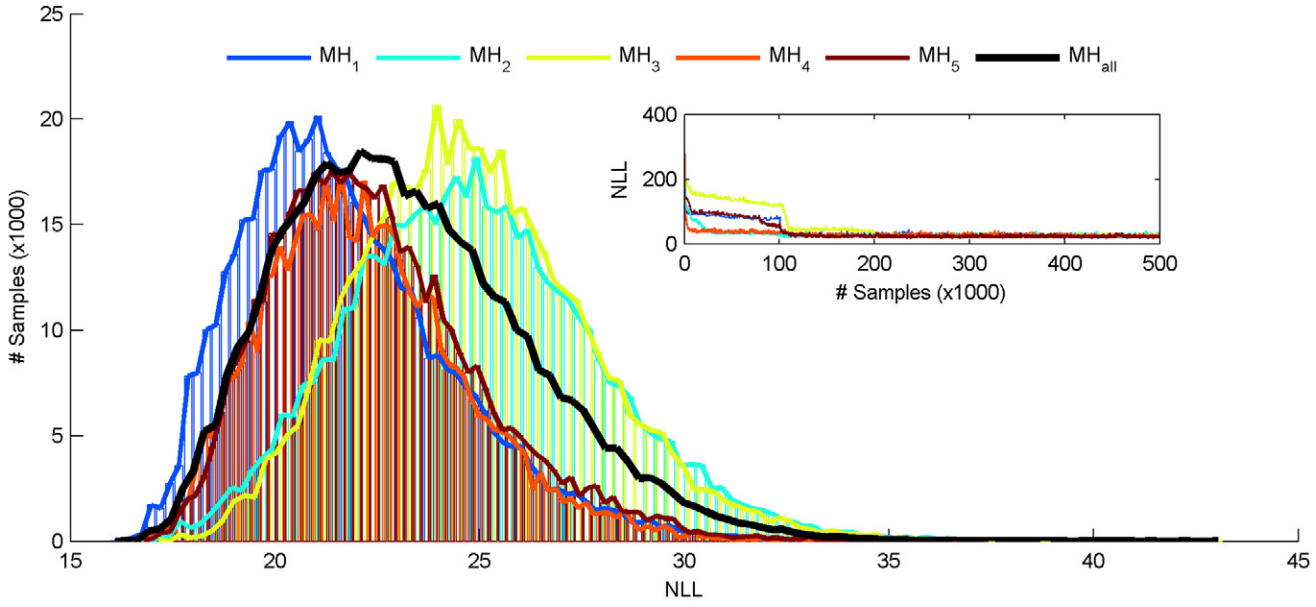

Fig. 11. Distributions of negative log likelihood (NLL) for all five Metropolis–Hastings (MH) chains excluding burn-in; the thick black line is the distribution from all five chains (MH_{all}). Inset: NLL evolution of the first 5×10^5 samples from individual chains including burn-in.

is ubiquitous in parameter inversion in general. In addition to looking at the one-dimensional distributions of parameters, we also looked at marginal (two-dimensional) distributions from MH_{all} and calculated correlation coefficients (R^2) between parameter pairs (Fig. 12). Figure 12 shows marginal distributions from MH_{all} only, but the trends in distributions and cross-correlation were similar for all individual chains and even subsets of chains (e.g., only samples with NLL < 25). The highest R^2 values for parameter pairs within the same material were found between θ_s–K_s in M1, M3, and M4 (R^2 = 0.97, 0.91, and 0.73, respectively), α–n in M1 and M3 (R^2 = 0.74 and 0.69, respectively), α–K_s in M1 (R^2 = 0.83), θ_s–n in M4 (R^2 = 0.62), and n–K_s in M2 (R^2 = 0.80). For all other pairs, R^2 values did not exceed 0.6. We show more explicitly below the effects of parameter correlation on the physical aspects of the VGM relationships and data fit.

Parameter Relationship to Soil Characteristic Curves

The Mo values presented in Table 3 represent only the most likely set of parameters given the data, the forward model, and the current sampling algorithm. Low NLL values despite wide distributions and high R^2 values between parameters imply that, for many parameters, there is a range of values that will fit the data equally well. What is controlling the distribution and movement of moisture within the soil, as depicted by the model, is the shape of the VGM $\theta(\psi)$ and $K(\psi)$ functions, and individual parameters can be considered curve-fitting parameters to these functions.

To investigate the effects of parameter uncertainty on uncertainty in the $\theta(\psi)$ and $K(\psi)$ functions, we randomly chose 2000 parameter sets from MH_{all} and plotted 2000 different $\theta(\psi)$ and log $K(\psi)$ characteristic curves for each of the four materials (Fig. 13). Despite the wide range of individual parameters chosen (σ^2 values of the sets chosen were similar to the σ^2 values presented in Table 3), we see that the relationships between parameters, whether two or higher dimension, combine to produce $\theta(\psi)$ and $K(\psi)$ functions that are representative of realistic VGM functions and, especially for M1 and M4, are unique and informative, with well-defined shapes that are very near the curve shapes typical of standard agricultural soils (the clear exceptions being M2 functions, which indicates the model's insensitivity to that material's properties). Stauffer and Lu (2012) made a similar inference that curve shapes are more informative than individual parameters (due to parameter cross-correlation) and used this to reduce computation time in unsaturated flow modeling.

The successful application of the VGM model and the finding that curve shapes and parameter values typical of sand soils can be used to describe the in situ flow behavior of this conglomeratic alluvial soil implies that more complicated models, such as those with corrections to unsaturated soil models (e.g., Bouwer and Rice, 1984; Peck and Watson, 1979) or separation of the relatively fine-grained fraction from the coarse fraction (e.g., Tetegan et al., 2011; Dann et al., 2009), and the associated additional model parameters, are not necessary to characterize unsaturated flow in conglomeratic alluvial soil, particularly under natural recharge conditions and where saturation values are low.

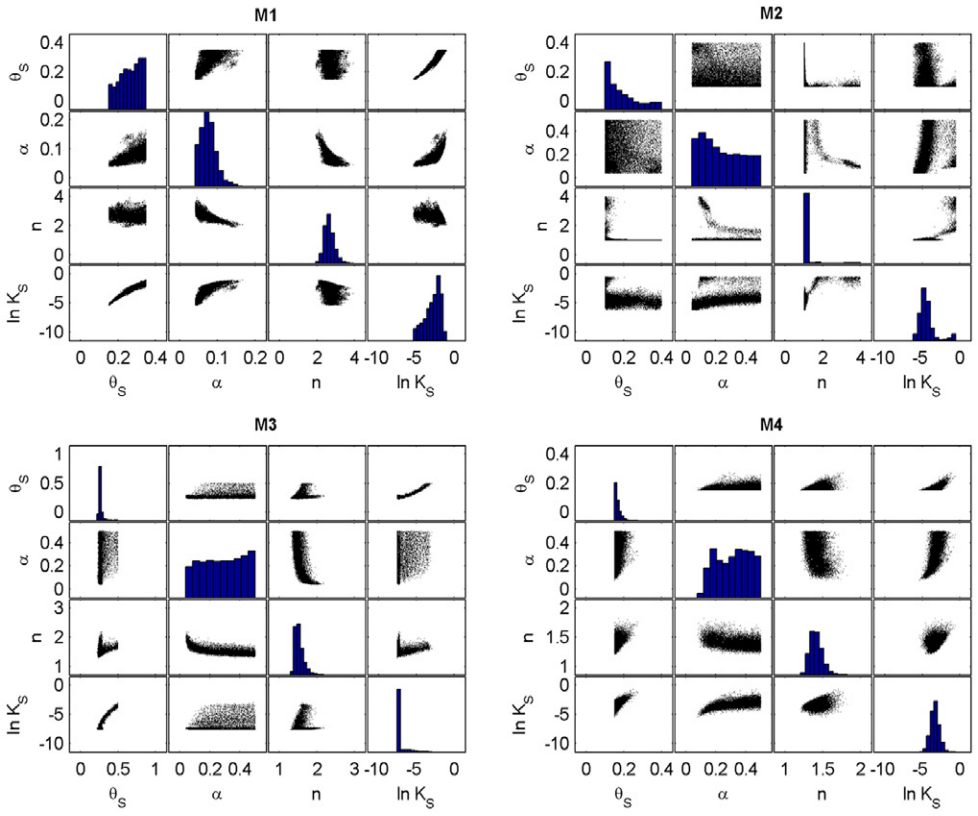

Fig. 12. Marginal distributions of saturated moisture content (θ_s), curve shape parameters α and n, and saturated hydraulic conductivity (K_s) from sets 5×10^5 through 1×10^6 of all Metropolis–Hastings (MH) chains combined for each material M1 to M4.

Figure 13 also emphasizes the relationship between parameter predictability and the saturation range of the experiment. Final θ values from the experiment were only about half the estimated θ_s (50% saturation) in Materials M1 and M4, and Fig. 13 shows that more of the 2000 $\theta(\psi)$ and $K(\psi)$ curves diverge near saturation, with the most clear example coming from M1. Less agreement

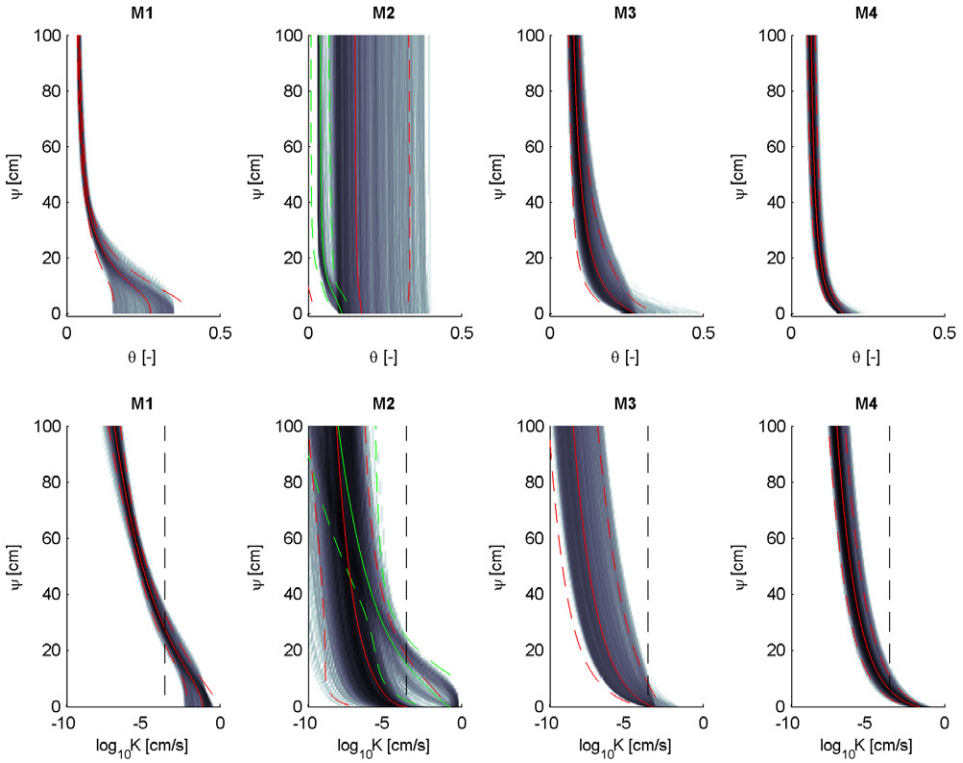

Fig. 13. Soil moisture $\theta(\psi)$ and hydraulic conductivity $K(\psi)$ curves produced from 2000 randomly chosen parameter sets from all five Metropolis–Hastings chains for each material M1 to M4. Darker shades indicate where more of the curves overlap; solid red lines represent mean curve values, and dashed red lines represent $\pm 2\sigma$. Green lines for M2 (sand) curves are from the second chain (MH_2) parameter sets only.

at high saturation implies poor resolution of the parameters that influence that portion of the curve: mainly θ_s and K_s. When not constrained by the observed data, θ_s and K_s represent only the end points of the curves and thus will be difficult to resolve without outside constraint (e.g., independent estimates), a conclusion also reached by Scharnagl et al. (2011). A similar case can be made for α, which relates to the bubbling pressure or the ψ value at which θ begins to decrease from saturation. If near-saturation is not reached, α may also be difficult to resolve, as is evident from the distributions shown in Fig. 10. Had the experiment covered the full range of saturation, θ_s and α would become more resolved and, given the high correlation between θ_s and other parameters (especially K_s), many other parameters would probably be better resolved as well. Fortunately, saturated parameters like θ_s and K_s can be easily and accurately obtained from other methods or experiments (e.g., neutron porosity logs, slug tests, pump tests, etc.), which can be used to constrain unsaturated models when full saturation is not reached.

The $\theta(\psi)$ and $K(\psi)$ curves shown in Fig. 13 also indicate the insensitivity of the model to M2—not only to individual M2 parameters, but to the shape of the full $\theta(\psi)$ and $K(\psi)$ functions. The wide distribution on the M2 $\theta(\psi)$ curves, but still low NLL values, shows that the forward model and calculated data are insensitive to M2 and that given the field experiment (and likely violation of one-dimensional assumptions for M2 especially), the model will struggle to resolve M2 parameters in its current capacity. This is not surprising given that θ measurements were not made within M2 and, according to the installation depths of AT8, ψ measurements were made very near the top of the material zone (see Fig. 9). Had the sensor been located lower in the material, the observed $\psi(t)$ data would have been more influenced by the M2 $\theta(\psi)$ and $K(\psi)$ functions because water would have to flow through more of that material before reaching the sensor. Interestingly, if we were to look only at the $\theta(\psi)$ and $K(\psi)$ curves produced from chain MH_2 (μ and σ of the curves shown in Fig. 13), which maintained a higher Mo for n_{M2} and $K_{s,M2}$ for much of the last 5×10^5 runs, the $\theta(\psi)$ and $K(\psi)$ curves have much better agreement and have a shape more similar to typical soils (i.e., a clearly defined curve and bubbling pressure). It is possible that the higher n and K_s values initially predicted by MH_2, because of the initial parameter set, were due to the sampling algorithm becoming temporarily trapped in a local minimum. As MH_2 progressed further, it began to approach the global minimum approached by the other chains. Had we stopped the algorithm too soon or used only the results from MH_2, we would have predicted higher n and K_s values and more informative $\theta(\psi)$ and $K(\psi)$ curves but would have overestimated the dependence of the model to parameters n_{M2} and $K_{s,M2}$ and underestimated the parameter uncertainty.

In Fig. 13, we show how the range of optimal parameters predicted by the MH sampling produced wide distributions of some parameters but that those parameters still work together to produce informative $\theta(\psi)$ and $K(\psi)$ relationships across the range of saturation achieved by the experiment (a similar concept to that of Stauffer and Lu, 2012). To show the model's ability to reproduce the observed $\psi(t)$ and $\theta(t)$ data from the experiment, we took a similar approach as in Fig. 13 of using a random sample of parameter sets from within the final distributions. In Fig. 14, we show fits to observed $\psi(t)$ and $\theta(t)$ data for 2000 forward model runs using randomly chosen parameter sets. Figure 14 further emphasizes that uncertainty in input parameters does not necessarily correlate to uncertainty in the calculated data or negate the model's ability to capture the observed behavior and shows that uncertainty in

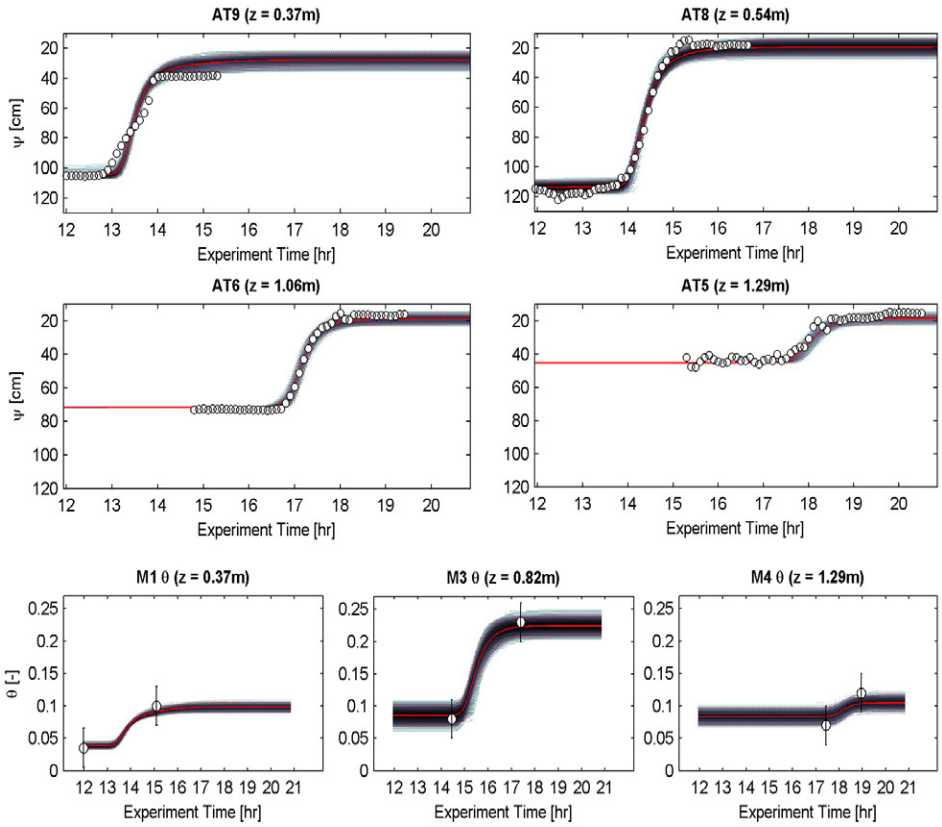

Fig. 14. Soil tension $\psi(t)$ and moisture $\theta(t)$ intensity plots calculated from 2000 parameter sets taken from all five Metropolis–Hastings chains (MH_{all}) for the four observed advanced tensiometer (AT) and three moisture (M) measurement depths. Darker shades indicate where more of the curves overlap. Solid red lines are mean values and dashed red lines are $\pm 2\sigma$; white circles are observed data.

parameters, or the lack of full model convergence, does not lead to high uncertainty in the predicted data.

Summary and Conclusions

Artificial rain was applied to a 5- by 2-m area using standard greenhouse misters at an average rate of 0.84 cm h^{-1} for 19 h until vertical $\theta(z)$ and $\psi(z)$ profiles reached steady state. A one-dimensional unsaturated flow model was used to predict $\psi(t)$ at four observation depths and θ_{dry} and θ_{wet} for three specific layers. Five independent MH sampling algorithms with 10^6 samples each were used to identify the distributions of in situ parameters for the VGM relationships of four materials in the test site sediment sequence. Several types of information were gathered before the test for better planning of the experiment and to provide useful prior information for model development and initial optimization parameters. The model material distribution and initial model properties (e.g., stratigraphy, boundary conditions, and initial parameter values) were estimated from GPR reflection data, soil core samples, and long-term monitoring before the experiment.

Optimal NLL values predicted by the five independent MH chains were reached after $\sim 3 \times 10^5$ samples for all chains and remained between 15 and 35 through 1.5×10^6 samples. Final parameter distributions from the last 5×10^5 samples of the five separate MH chains produced similar mode values, and only 11 of the 16 parameter distributions produced final SR values <1.2, which implies a lack of convergence of the full model. We attribute model non-convergence to the high variability of the NLL functions for certain parameters (e.g., nonlinearity, several local minima, etc.) and high correlation between parameters. Furthermore, we feel that this lack of convergence is an unavoidable aspect of the data set and expresses the difficulty with in situ methods and inherent uncertainty in the VGM functions used under specific conditions [i.e., heterogeneity and the use of only $\psi(t)$ data to constrain parameters]. Marginal distributions and R^2 values showed that some material parameters were very highly correlated ($R^2 > 0.9$), specifically, θ_s–K_s and α–n. Despite the range of parameter values within individual and combined chains and the apparent lack of full model convergence, the $\theta(\psi)$ and $K(\psi)$ curves predicted by 2000 randomly chosen parameter sets were generally in agreement within the range of the observed ψ, θ, and K produced by the experiment and diverged as the curves approached saturation, which was not reached during the experiment. Similarly, $\psi(t)$ and $\theta(t)$ predicted from a random subset of all sets were in very good agreement with each other and with the observed data despite the wide distributions of some parameters, indicating complex parameter correlation and non-uniqueness.

Our results highlight the strong non-uniqueness of the unsaturated hydraulic properties of very coarse material specifically, and unsaturated materials in general, and the difficulty involved in obtaining a single ideal set of parameter values for a given material under natural field conditions, especially when one-dimensional assumptions are violated and optimal data are not collected for all materials. Gathering additional information, such as $\psi(t)$ and $\theta(t)$ in each material layer, covering the full range of saturation during the experiment (i.e., by applying precipitation at rates far exceeding natural conditions), or constraining the parameters with prior information would lead to tighter, more informative distributions of the VGM functions but would probably still be burdened by parameter cross-correlation and non-uniqueness.

In conclusion, this study (i) successfully applied a field-based infiltration experiment to characterize in situ unsaturated hydraulic

properties for a coarse (sand, gravel, and cobble), alluvial sediment sequence, (ii) showed that high infiltration rates (i.e., greater than natural precipitation rates for long periods) can be accommodated by conglomeratic soil despite relatively low porosities and high concentration of large cobbles (d > 20 cm), (iii) highlighted the difficulty in developing soil characteristic curves for coarse soil types under natural infiltration conditions, given that moisture levels may not reach saturation and thus certain parameters like θ_s and K_s will be difficult to resolve, and (iv) suggested that soil characteristic functions developed for fine-grained agricultural soils, such as VGM relationships, can be successfully applied to predict in situ unsaturated flow behavior of cobble-dominated alluvial soils.

Acknowledgments

This work was supported by the U.S. Army RDECOM ARL Army Research Office under Grant W911NF-09-1-0534. We would also like to thank Brady Johnson, Josh Ekhoff, Pam Aishlin, and Andreas Meyer for help during the experiment and Dr. Joel Hubbell of the Idaho National Laboratory and Jerry Noe of Electronic Engineering Innovations for assistance with design modifications, tuning, and installation of the advanced tensiometers.

References

Abbasi, F., D. Jacques, J. Šimůnek, J. Feyen, and M.Th. van Genuchten. 2003. Inverse estimation of soil hydraulic and transport parameters from transient field experiments: Heterogeneous soil. Trans. ASAE 46:1097–1111.

Aishlin, P., M. Thoma, and W. Barrash. 2013. Installation, maintenance, and offset calculation for tensiometers at the Boise Hydrogeophysical Research Site. CGISS Tech. Rep. 13-02. Boise State Univ., Boise, ID

Barrash, W., and T. Clemo. 2002. Hierarchical geostatistics and multifacies systems: Boise Hydrogeophysical Research Site, Boise, Idaho. Water Resour. Res. 38(10):1196. doi:10.1029/2002WR001436

Barrash, W., T. Clemo, J.J. Fox, and T.C. Johnson. 2006. Field, laboratory, and modeling investigation of the skin effect at wells with slotted casing, Boise Hydrogeophysical Research Site. J. Hydrol. 326:181–198. doi:10.1016/j.jhydrol.2005.10.029

Barrash, W., T. Clemo, and M. Knoll. 1999. Boise Hydrogeophysical Research Site (BHRS): Objectives, design, initial geostatistical results. In: Proceeding of SAGEEP99, the Symposium on the Application of Geophysics to Engineering and Environmental Problems, Oakland, CA. 14–18 Mar. 1999. Eng. Environ. Geophys. Soc., Denver, CO. p. 389–398

Barrash, W., and E.C. Reboulet. 2004. Significance of porosity for the stratigraphy and textural composition in subsurface fluvial deposits, Boise Hydrogeophysical Research Site. Geol. Soc. Am. Bull. 116:1059–1073. doi:10.1130/B25370.1

Bouwer, H., and R.C. Rice. 1984. Hydraulic properties of stoney vadose zones. Ground Water 22:696–705. doi:10.1111/j.1745-6584.1984.tb01438.x

Bradford, J., W. Clement, and W. Barrash. 2009. Estimating porosity with ground-penetrating radar reflection tomography: A controlled 3-D experiment at the Boise Hydrogeophysical Research Site. Water Resour. Res. 45:W00D26. doi:10.1029/2008WR006960

Cardiff, M., W. Barrash, and P.K. Kitanidis. 2012. A field proof-of-concept of aquifer imaging using 3D transient hydraulic tomography with modular, temporally-emplaced equipment. Water Resour. Res. 48:W05531. doi:10.1029/2011WR011704

Cardiff, M., W. Barrash, M. Thoma, and B. Malama. 2011. Information content of slug tests for estimating hydraulic properties in realistic, high-conductivity aquifer scenarios. J. Hydrol. 403:66–82. doi:10.1016/j.jhydrol.2011.03.044

Carsel, R.F., and R.S. Parrish. 1988. Developing joint probability distributions of soil water retention characteristics. Water Resour. Res. 24:755–769. doi:10.1029/WR024i005p00755

Cassel, D., and A. Klute. 1986. Water potential: Tensiometry. In: A. Klute, editor, Methods of soil analysis. Part 1. Physical and mineralogical methods. 2nd ed. Agron. Monogr. 9. ASA and SSSA, Madison, WI. p. 563–596.

Cerdá, A. 2001. Effects of rock fragment cover on soil infiltration, interrill runoff and erosion. Eur. J. Soil Sci. 52:59–68. doi:10.1046/j.1365-2389.2001.00354.x

Clement, W.P., and W. Barrash. 2006. Crosshole radar tomography in a fluvial aquifer near Boise, Idaho. J. Environ. Eng. Geophys. 11:171–184. doi:10.2113/JEEG11.3.171

Clement, W.P., W. Barrash, and M.D. Knoll. 2006. Reflectivity modeling of a ground-penetrating-radar profile of a saturated fluvial formation. Geophysics 71:K59–K66. doi:10.1190/1.2194528

Corwin, D., K. Loague, and T. Ellsworth. 1999. Assessment of non-point source pollution in the vadose zone. Geophys. Monogr. 108. Am. Geophys. Union, Washington, DC.

Cousin, I., B. Nicoullaud, and C. Coutadeur. 2003. Influence of rock fragments on the water retention and water percolation in a calcareous soil. Catena 53:97–114. doi:10.1016/S0341-8162(03)00037-7

Dafflon, B., J. Irving, and W. Barrash. 2011. Inversion of multiple intersecting high-resolution crosshole GPR profiles for hydrological characterization at the Boise Hydrogeophysical Research Site. J. Appl. Geophys. 73:305–314. doi:10.1016/j.jappgeo.2011.02.001

Dann, R., M. Close, M. Flintoft, R. Hector, H. Barlow, S. Thomas, and G. Francis. 2009. Characterization and estimation of hydraulic properties in an alluvial gravel vadose zone. Vadose Zone J. 8:651–663. doi:10.2136/vzj2008.0174

Dunn, A.J., and G.R. Mehuys. 1982. Relationship between gravel content of soils and saturated hydraulic conductivity in laboratory tests. In: J.D. Nichols et al., editors, Erosion and productivity of soils containing rock fragments. SSSA Spec. Publ. 13. SSSA, Madison, WI. p. 55–63. doi:10.2136/sssaspecpub13.c6

Edwards, W.M., P.F. Germann, L.B. Owens, and C.R. Amerman. 1984. Watershed studies of factors influencing infiltration, runoff, and erosion on stony and non-stony soils. In: J.D. Nichols et al., editors, Erosion and productivity of soils containing rock fragments. SSSA Spec. Publ. 13. SSSA, Madison, WI. p. 45–54. doi:10.2136/sssaspecpub13.c5

Gelman, A., and D.B. Rubin. 1992. Inference from iterative simulation using multiple sequences. Stat. Sci. 7:457–472. doi:10.1214/ss/1177011136

Hastings, W.K. 1970. Monte Carlo sampling methods using Markov chains and their applications. Biometrika 57:97–109. doi:10.1093/biomet/57.1.97

Hendrickx, J.M.H., A.S. Khan, M.H. Bannink, D. Birch, and C. Kidd. 1991. Numerical analysis of groundwater recharge through stony soils using limited data. J. Hydrol. 127:173–192. doi:10.1016/0022-1694(91)90114-W

Hubbell, J.M., and J.B. Sisson. 1998. Advanced tensiometer for shallow or deep soil-water pressure measurements. Soil Sci. 163:271–277. doi:10.1097/00010694-199804000-00002

Inoue, M., J. Šimůnek, J.W. Hopmans, and V. Clausnitzer. 1998. In situ estimation of soil hydraulic functions using a multistep soil-water extraction technique. Water Resour. Res. 34:1035–1050. doi:10.1029/98WR00295

Johnson, B., B. Malama, W. Barrash, and A.N. Flores. 2013a. Recognizing and modeling variable drawdown due to evapotranspiration in a semiarid riparian zone considering local differences in vegetation and distance from a river source. Water Resour. Res. 49:1030–1039. doi:10.1002/wrcr.20122

Johnson, B., M. Thoma, and W. Barrash. 2013b. Neutron probe installation, calibration, and data treatment at the BHRS. CGISS Tech. Rep. 13-01. Boise State Univ., Boise, ID.

Laloy, E., M. Weynants, C.L. Bielders, M. Vanclooster, and M. Javaux. 2010. How efficient are one-dimensional models to reproduce the hydrodynamic behavior of structured soils subjected to multi-step outflow experiments? J. Hydrol. 393:37–52. doi:10.1016/j.jhydrol.2010.02.017

Leij, F.J., W.J. Alves, M.Th. van Genuchten, and J.R. Williams. 1996. Unsaturated soil hydraulic database: UNSODA 1.0 user's manual. Rep. EPA/600/R-96/095. USEPA, Ada, OK

Liu, X., M.A. Cardiff, and P.K. Kitanidis. 2010. Parameter estimation in nonlinear environmental problems. Stochastic Environ. Res. Risk Assess. 24:1003–1022. doi:10.1007/s00477-010-0395-y

Ma, D., M. Shao, J. Zhang, and Q. Wang. 2010. Validation of an analytical method for determining soil hydraulic properties of stony soils using experimental data. Geoderma 159:262–269. doi:10.1016/j.geoderma.2010.08.001

Malama, B., W. Barrash, M. Cardiff, M. Thoma, and K. Kuhlman. 2011. Modeling slug tests in unconfined aquifers taking into account water table kinematics, wellbore skin, and inertial effects. J. Hydrol. 408:113–126. doi:10.1016/j.jhydrol.2011.07.028

Malama, B., and B. Johnson. 2010. Analytical modeling of saturated zone head response to evapotranspiration and river stage fluctuations. J. Hydrol. 382:1–9. doi:10.1016/j.jhydrol.2009.12.010

Mehuys, G.R., L.H. Stolzy, J. Letey, and L.V. Weeks. 1975. Effects of stones on the hydraulic conductivity of relatively dry desert soils. Soil Sci. Soc. Am. J. 39:37–42. doi:10.2136/sssaj1975.03615995003900010013x

Metropolis, N., A.W. Rosenbluth, M.N. Rosenbluth, A.H. Teller, and E. Teller. 1953. Equation of state calculations by fast computing machines. J. Chem. Phys. 21:1087–1092.

Milczarek, M.A., D. Zyl, S. Peng, and R. Rice. 2006. Saturated and unsaturated hydraulic properties characterization at mine facilities: Are we doing it right? In: Proceedings of the 7th International Conference on Acid Rock Drainage, St. Louis, MO. 26–30 Mar. 2006. Am. Soc. Min. Reclam., Lexington, KY. p. 1273–1286.

Miller, F.T., and R.L. Guthrie. 1984. Classification and distribution of soils containing rock fragments in the United States. In: J.D. Nichols et al., editors, Erosion and productivity of soils containing rock fragments. SSSA Spec. Publ. 13. SSSA, Madison, WI. p. 1–6. doi:10.2136/sssaspecpub13.c1

Moret, G.J., M.D. Knoll, W. Barrash, and W.P. Clement. 2006. Investigating the stratigraphy of an alluvial aquifer using crosswell seismic traveltime tomography. Geophysics 71(3):B63–B73. doi:10.1190/1.2195487

Mwenifumbo, C.J., W. Barrash, and M.D. Knoll. 2009. Capacitive conductivity logging and electrical stratigraphy in a high-resistivity aquifer, Boise Hydrogeophysical Research Site. Geophysics 74(3):E125–E133. doi:10.1190/1.3106760

Oostrom, M., G.D. Tartakovsky, T.W. Wietsma, M.J. Truex, and J.H. Dane. 2011. Determination of water saturation in relatively dry porous media using gas-phase traced tests. Vadose Zone J. 10:634–641. doi:10.2136/vzj2010.0101

Oostrom, M., T.W. Wietsma, J.H. Dane, M.J. Truex, and A.L. Ward. 2009. Desiccation of unsaturated porous media: Intermediate-scale experiments and numerical simulation. Vadose Zone J. 8:643–650. doi:10.2136/vzj2008.0182

Peck, A.J., and J.D. Watson. 1979. Hydraulic conductivity and flow in non-uniform soil. In: Workshop on Soil Physics and Field Heterogeneity: Working Papers, Canberra, Australia. 12–14 Feb. 1979. CSIRO Div. of Environ. Mech., Canberra, ACT, Australia. p. 31–39.

Rawls, W.J., D.L. Brakensiek, and K.E. Saxton. 1982. Estimation of soil water properties. Trans. ASAE 25:1316–1320. doi:10.13031/2013.33720

Reboulet, E.C., and W. Barrash. 2003. Core, grain size, and porosity data from the BHRS. CGISS Tech. Rep. 03-02. Boise State Univ., Boise, ID.

Ritter, A., F. Hupet, R. Muñoz-Carpena, S. Lambot, and M. Vanclooster. 2003. Using inverse methods for estimating soil hydraulic properties from field data as an alternative to direct methods. Agric. Water Manage. 59:77–96. doi:10.1016/S0378-3774(02)00160-9

Sauer, T.J., and S.D. Logsdon. 2002. Hydraulic and physical properties of stony soils in a small watershed. Soil Sci. Soc. Am. J. 66:1947–1956. doi:10.2136/sssaj2002.1947

Scharnagl, B., J.A. Vrugt, H. Vereecken, and M. Herbst. 2011. Inverse modeling of in situ soil water dynamics: Investigating the effect of different prior distributions of the soil hydraulic parameters. Hydrol. Earth Syst. Sci. 15:3043–3059. doi:10.5194/hess-15-3043-2011

Šimůnek, J., R. Angulo-Jaramillo, M.G. Schaap, J.-P. Vandervaere, and M.Th. van Genuchten. 1998. Using an inverse method to estimate the hydraulic properties of crusted soils from tension-disc infiltrometer data. Geoderma 86:61–81. doi:10.1016/S0016-7061(98)00035-4

Šimůnek, J., M.Th. van Genuchten, and M. Šejna. 2005. The HYDRUS-1D software package for simulating the one-dimensional movement of water, heat, and multiple solutes in variably-saturated media. Dep. of Environ. Sci., Univ. of California, Riverside.

Sisson, J.B., G.W. Gee, J.M. Hubbell, W.L. Bratton, J.C. Ritter, A.L. Ward, and T.G. Caldwell. 2002. Advances in tensiometry for long-term monitoring of soil water pressures. Vadose Zone J. 1:310–315. doi:10.2136/vzj2002.3100

Slater, L., A. Binley, W. Barrash, J. Keery, J. Montrey, and M. Cardiff. 2011. An investigation of the ability of induced polarization to resolve aquifer heterogeneity in an unconsolidated sedimentary aquifer. In: Abstracts, SAGEEP: the Symposium on the Application of Geophysics to Engineering and Environmental Problems, Charleston, SC. 10–14 Apr. 2011. Soc. Explor. Geophys., Tulsa, OK.

Stauffer, P.H., and A. Lu. 2012. Quantifying transport uncertainty in unsaturated rock using Monte Carlo sampling of retention curves. Vadose Zone J. 11(4). doi:10.2136/vzj2011.0171

Straface, S., F. Chidichima, M. Rizzo, W. Barrash, A. Revil, M. Cardiff, and A. Guadagini. 2011. Joint inversion of steady-state hydrologic and self-potential data for 3D hydraulic conductivity distribution at the Boise Hydrogeophysical Research Site. J. Hydrol. 407:115–128. doi:10.1016/j.jhydrol.2011.07.013

Tarantola, A. 2005. Inverse problem theory and methods for model parameter estimation. Soc. Ind. Appl. Math., Philadelphia, PA.

Tetegan, M., B. Nicoullaud, D. Baize, A. Bouthier, and I. Cousin. 2011. The contribution of rock fragments to the available water content of stony soils: Proposition of new pedotransfer functions. Geoderma 165:40–49. doi:10.1016/j.geoderma.2011.07.001

Tokunaga, T.K., K.R. Olson, and J. Wan. 2003. Moisture characteristics of Hanford gravels: Bulk, grain-surface, and intragranular components. Vadose Zone J. 2:322–329.

van Genuchten, M.Th. 1980. A closed form equation for predicting the hydraulic conductivity of unsaturated soils. Soil Sci. Soc. Am. J. 44:892–898.

Vrugt, J.A., and W. Bouten. 2002. Validity of first-order approximations to describe parameter uncertainty in soil hydrologic models. Soil Sci. Soc. Am. J. 66:1740–1751. doi:10.2136/sssaj2002.1740

Vrugt, J.A., W. Bouten, H.V. Gupta, and J.W. Hopmans. 2003a. Toward improved identifiability of soil hydraulic parameters: On the selection of a suitable parametric model. Vadose Zone J. 2:98–113.

Vrugt, J.A., H.V. Gupta, W. Bouten, and S. Sorooshian. 2003b. A Shuffled Complex Evolution Metropolis algorithm for optimization and uncertainty assessment of hydrologic model parameters. Water Resour. Res. 39:1201. doi:10.1029/2002WR001642

Wohling, T., and J.A. Vrugt. 2011. Multiresponse multilayer vadose zone model calibration using Markov chain Monte Carlo simulation and field water retention data. Water Resour. Res. 47:W04510. doi:10.1029/2010WR009265

Zhang, L., and Q. Chen. 2005. Predicting bimodal soil-water characteristic curves. J. Geotech. Geoenviron. Eng. 131:666–670. doi:10.1061/(ASCE)1090-0241(2005)131:5(666)

Zhang, Z.F., A.L. Ward, and J.M. Keller. 2011. Determining the porosity and saturated hydraulic condictivity of binary mixtures. Vadose Zone J. 10:313–321. doi:10.2136/vzj2009.0138

Zou, Z.-Y., M.H. Young, Z. Li, and P.J. Wierenga. 2001. Estimation of depth averaged unsaturated soil hydraulic properties from infiltration experiments. J. Hydrol. 242:26–42. doi:10.1016/S0022-1694(00)00385-1